Steel and Composite Structures, *Vol. 38, No. 4 (2021) 381-397*
DOI: https://doi.org/10.12989/scs.2021.38.4.381

Hybrid simulation tests of high-strength steel composite K-eccentrically braced frames with spatial substructure

Tengfei Li[1a], Mingzhou Su*[1,2] and Jiangran Guo[1b]

[1]School of Civil Engineering, Xi'an University of Architecture and Technology, Xi'an 710055, P.R. China
[2]Key Lab of Structural Engineering and Earthquake Resistance, Ministry of Education (XAUAT), Xi'an 710055, P.R. China

(*Received May 6, 2019, Revised January 29, 2021, Accepted January 31, 2021*)

Abstract. Based on the spatial substructure hybrid simulation test (SHST) method, the seismic performance of a high-strength steel composite K-eccentrically braced frame (K-HSS-EBF) structure system is studied. First, on the basis of the existing pseudostatic experiments, a numerical model corresponding to the experimental model was established using OpenSees, which mainly simulated the shear effect of the shear links. A three-story and five-span spatial K-HSS-EBF was taken as the prototype, and SHST was performed with a half-scale SHST model. According to the test results, the validity of the SHST model was verified, and the main seismic performance indexes of the experimental substructure under different seismic waves were studied. The results show that the hybrid simulation results are basically consistent with the numerical simulation results of the global structure. The deformation of each story is mainly concentrated in the web of the shear link owing to shear deformation. The maximum interstory drifts of the model structure during *Strength Level Earthquake* (SLE) and *Maximum Considered Earthquake* (MCE) meet the demands of interstory limitations in the Chinese seismic design code of buildings. In conclusion, the seismic response characteristics of the K-HSS-EBFs are successfully simulated using the spatial SHST, which shows that the K-HSS-EBFs have good seismic performance.

Keywords: hybrid simulation; spatial substructure; high-strength steel; eccentrically braced frames; shear link

1. Introduction

Eccentrically braced frames (EBFs) are a structural system whose braces deviate from beam-column joints and have excellent seismic performance (Berman and Bruneau 2008, Bosco and Rossi 2009, Bosco and Rossi 2013, Ioana *et al*. 2016, Montuori *et al*. 2014, Shayanfar *et al*. 2011). The EBF system combines the advantages of the high ductility of moment-resisting frames (MRFs) and high strength of concentrically braced frames (CBFs). During an earthquake, EBFs dissipate seismic energy mainly by plastic deformation of the links. The current standard GB 50011-2010 stipulates that the steel yield strength of the link section of EBFs should not be greater than 345 MPa. The non-energy dissipation members such as frame beams and columns are designed by the method of the internal force amplification factor, which results in a large section of non-energy dissipation members and restricts the application and promotion of the EBFs.

High-strength steel (HSS), also known as high-performance steel (HPS), generally refers to steel with a yield strength greater than 460 MPa and a better yield platform, toughness, and weldability than conventional steel. Under the same design conditions, HSS can reduce the cross sections of components, save on materials, and reduce costs. HSS has good economic benefits and application prospects (Lian *et al*. 2015). At present, researchers have carried out detailed studies on the mechanical properties of HSS structural members (Alhendi and Celikag 2015, Aslani *et al*. 2016, Ban *et al*. 2013, Kim *et al*. 2014, Shi *et al*. 2012).

High-strength steel composite eccentrically braced frames (HSS-EBFs) combine the advantages of the high bearing capacity of HSS and good seismic performance of EBFs, so they have good engineering application prospects. During the high seismic intensity earthquakes, links with lower-yield-point steel (e.g., Q235 or Q345 steel with a nominal yield strength of 235 and 345 MPa, respectively) fully develop plastic energy dissipation, while members such as frame beams and columns retain their elasticity or develop slight plasticity owing to the use of high-strength steel.

Y-shaped HSS-EBF (Y-HSS-EBF) and K-shaped HSS-EBF (K-HSS-EBF) are the two most common types of HSS-EBF (see Fig.1). The shear link of the former is arranged between the lower flange of the frame beam and the brace node, while the latter is arranged in the plane of the frame beam and connected with the cross section of the frame beam. Compared with the former, the latter has two main advantages. Firstly, the lateral stiffness of K-HSS-EBF is larger than that of Y-HSS-EBF, because the shear link of Y-HSS-EBF is located outside the frame beam. Secondly, unlike K-HSS-EBF, the out of plane instability may occur at

*Corresponding author, Professor
E-mail: sumingzhou@xauat.edu.cn
[a]Ph.D. Student
E-mail: litengfei0217@163.com
[b]Ph.D. Student
E-mail: guocheng9229@163.com

ISSN: 1229-9367 (Print), 1598-6233 (Online)

the juncture of the three branches of Y-HSS-EBF without lateral support after link yielded (Wang *et al*. 2016). In recent years, the K-HSS-EBF system has attracted more attention of some researchers. Dubina *et al*. (2008) carried out a pseudostatic test composite K-shaped EBFs with different strengths of steel. The links were bolted to the frame beams, and a comparative analysis of the steel composite situation was conducted. Li *et al*. (2018) carried out a cyclic test loading of a three-story half-scale K-HSS-EBF, and compared the ductility, link rotations, and failure mode of all models with different link lengths using nonlinear dynamic analyses. Tian *et al*. (2018) performed half-scale three-story shake-table tests to investigate the dynamic characteristics of K-HSS-EBFs.

The substructure hybrid simulation test (SHST) method is a new type of structure test technology given the development of the substructure pseudodynamic test (Dermitzakis and Mahin 1985) and general finite element (FE) software. A global structure is generally divided into two parts, in which the easily damaged part in an earthquake is used as an experimental substructure to carry out actual tests, and the remaining part of the structure is used as a numerical substructure to carry out numerical simulations through FE software. The data communication between the experimental and numerical substructures is carried out by SHST interface software to conduct a seismic response analysis of large and complex structures.

SHST avoids the problems of pure FE simulations, which cannot record the real stiffness changes in a structure; pseudostatic tests, which cannot consider the real seismic effect; the low calculation efficiency of the pseudodynamic test; and the scale effect and insufficient counterweight of the shaking table. SHST can complete large-scale or even full-scale model tests (Wang *et al*. 2012, Khan *et al*. 2018, Li *et al*. 2020). When loading in real time, the influence of acceleration on the test model can also be considered (Chae *et al*. 2015, Wu *et al*. 2016, Fu *et al*. 2019).

In order to further investigate the seismic performance of K-HSS-EBFs, the spatial SHST method proposed by Li *et al*. (2019) was adopted. On the basis of existing pseudostatic experiments, an FE model corresponding to the experimental model was established by using OpenSees, and the validity of the model was verified to ensure the effectiveness of the numerical substructure in SHST.

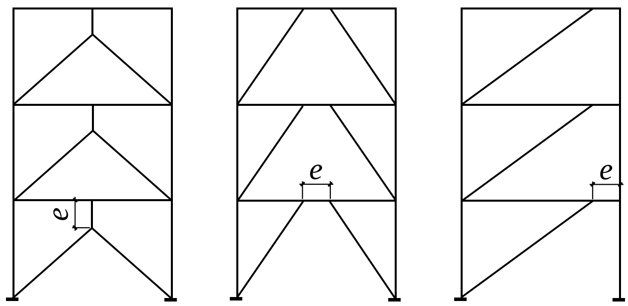

Fig. 1 The typical layout of HSS-EBF

Then, a three-story and five-span spatial K-HSS-EBF was taken as a prototype. SHST was carried out with the half-scale SHST model. The test results verified the validity of the SHST model, and the main seismic performance indexes of the experimental substructure under different seismic waves were studied.

2. Verification of FE model

A low-cyclic loading test of a three-story K-HSS-EBF in half scale was carried out by Li *et al*. (2018). The links were shear-yielding beams with a length of 350 mm. As shown in Fig. 2, the story height was 1800 mm, and the span in both directions was 2825 mm. Table 1 lists the sectional dimensions and steel types of the specimen. In this test, MTS actuators were used to carry out vertex horizontal loading, and a load-displacement hybrid control mode was adopted. The hysteretic behavior, energy dissipation capacity, stiffness degradation, and story drifts of the specimens were investigated.

The general FE software OpenSees was used to simulate the experimental model by Li *et al*. (2018). The concrete floor was assumed to be a rigid floor. The column foot and beam column joints were rigidly connected, and the braces were hinged.

2.1 Basic model parameters

The force beam-column elements, which can consider nonlinearity, are used to simulate the frame beams and columns. Truss elements with two hinged ends are used to simulate the braces. The simulation of shear links will be discussed in Section 2.2.

A fiber section is used to simulate the strong nonlinearity of the members. Steel02 (Menegotto 1973), a uniaxial constitutive material with isotropic strain hardening and the Bauschinger effect, is chosen as the constitutive model for all steels. The yield strength f_y and modulus of elasticity E of the material were used as mean values of the material property tests by Li *et al*. (2018). The strain hardening rate b is 0.02. The shape control parameters of the three-curve transition section R_0, cR_1, cR_2 and the isotropic hardening parameters a_1–a_4 are discussed in reference to the OpenSees user manual (Mazzoni 2009). The specific values are listed in Table 2.

2.2 Modeling research of shear link

In order to better simulate the shear effect of the shear links, a zero-length element provided in OpenSees that can add shear material as used as a model. As shown in Fig. 3, when the shear link section yields under shear, the entire section almost enters plasticity at the same time. Referring to the simplified definition of a shear model by Ö zhendekci and Ö zhendekci (2008), the shear hinges are set at both ends of the shear link by using a zero-length element, assuming that shear deformation occurs only in hinges and that the bending and axial deformation are borne by the elastic element in the middle.

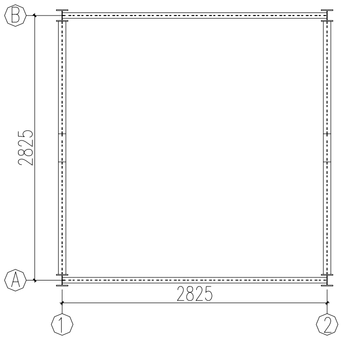

(a) Plan view

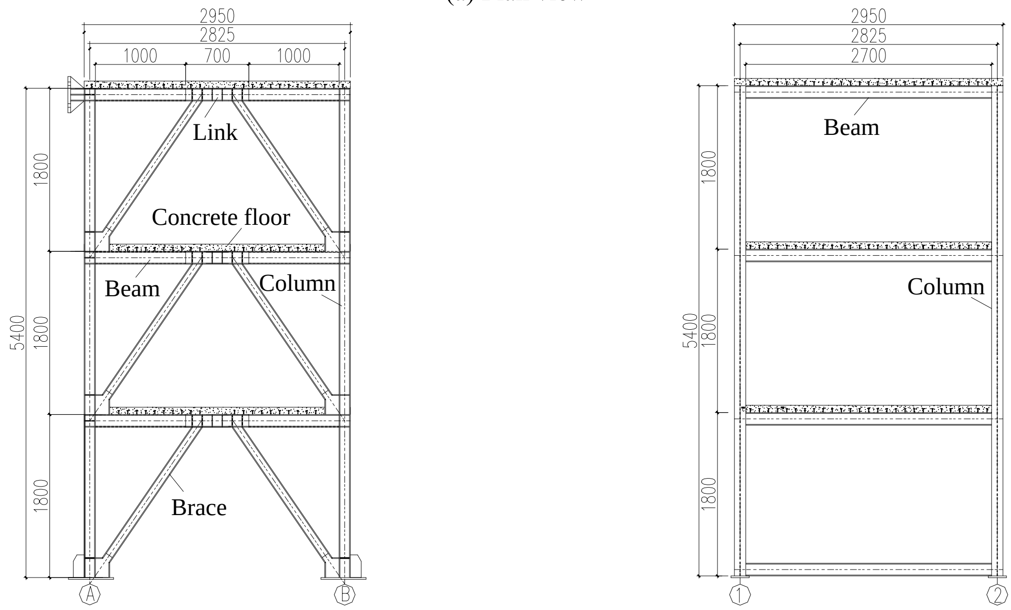

(b) Elevation view

Fig. 2 Test model

Table 1 Cross sectional dimensions of the model

Members	Cross section size/mm	Steel
Column	H125×125×8×10	Q460C
Beam	H140×100×8×10	Q460C
Brace	H100×100×6×10	Q345B
Shear link	H140×100×6×10	Q345B

Table 2 Parameters of Steel02

Steel	f_y/MPa	E/(10^5 MPa)	b	R_0	cR_1	cR_2	a_1	a_2	a_3	a_4
Q345B	389.25	2.06	0.02	18.5	0.925	0.1	0	1	0	1
Q460C	464.55	2.04	0.02	18.5	0.925	0.1	0	1	0	1

Zero-length element modeling determines the restoring force parameters of the shear direction spring reasonably. Steel02 material, which can consider the Bauschinger effect and isotropic strain hardening in modeling and analysis, is used in this study. In the zero-length element, the yield strength f_y of the Steel02 material corresponds to the yield shear force V_y of the shear link, and the elastic modulus E corresponds to the shear linear stiffness K_0 of the shear link.

For the yield shear of the cross section, the initial yield shear V_y as demarcated by Özhendekci and Özhendekci (2008) and the increase coefficient of flange shear α as considered by Yang (2011) are calculated in terms of Eqs. (1) and (2), respectively

$$V_y = 1.1\alpha V_p \tag{1}$$

where V_p is the yield shear force of the web of the shear link

$$\alpha = 1 + \frac{A_f^2 - 0.0625(et_w)^2}{0.58 A_w b_f e} \tag{2}$$

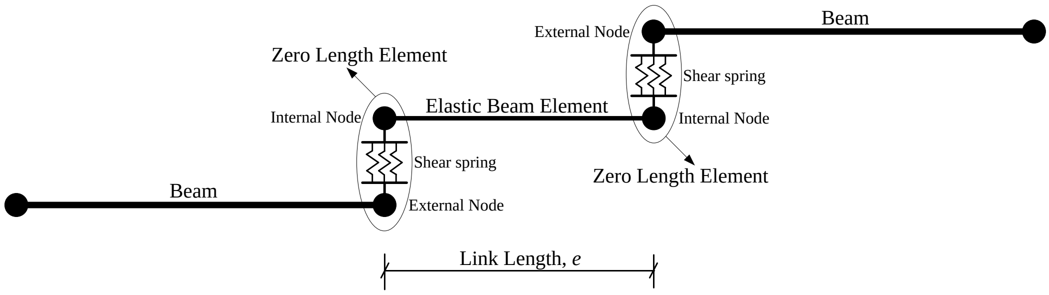

Fig. 3 Simplified model of shear link

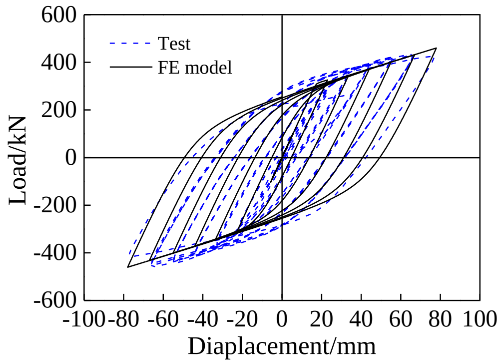

Fig. 4 Comparison of the hysteretic loops

where A_f is the cross-sectional area of a single flange of the shear link; e is the length of the shear link; t_w and A_w are the web thickness and web area of the shear link, respectively; and b_f is the width of the flange.

As shown in Fig. 3, since the shear springs in the plastic hinges at both ends of the beam are in series, the initial shear linear stiffness of the two springs is defined as

$$K_{0i}=K_{0j}=2GA_w/e \tag{3}$$

where G is the shear stiffness of the section and is equal to 80 GPa.

The equivalent shear stiffness of the shear link can be calculated as

$$K=1/K_{0i}+1/K_{0j}=GA_w/e \tag{4}$$

Based on Eqs. (1) and (4), the control parameters of the shear spring and the corresponding parameters of Steel02 are calculated and listed in Table 3. The other values are consistent with the material constitutive values in Table 2.

The uniaxial hysteresis loops of the FE model are compared with those of the test, as shown in Fig. 4. Because the Bauschinger effect can be considered in the Steel02 material, the load-displacement loops of the FE model and the test are basically consistent. Moreover, the FE model does not consider the restraint effect of the floor on the beam or the strengthening effect of the stiffener plate of the shear link, so the bearing capacity of the FE model is slightly lower than that of the test results.

The above analysis shows that the modeling method in this section can be used to simulate the numerical substructures of a SHST model.

3. SHST principle

In the SHST, the motion equation of the structure in step i can be proposed as

$$(M^a\ddot{X}_i+C^a\dot{X}_i+K^aX_i)+(M^e\ddot{X}_i+C^e\dot{X}_i+K^eX_i)=F_i \tag{5}$$

Where $\ddot{X}_i$, $\dot{X}_i$, and X_i are the acceleration, velocity, and displacement of the structure, respectively. M^a, C^a, and K^a are the mass, damping, and stiffness of the numerical substructure, respectively. M^e, C^e, and K^e are the mass, damping, and stiffness of the experimental substructure, respectively. F_i is the external exciting force.

The SHST principle is shown in Fig. 5. The response forces $M^a\ddot{X}_i$, $C^a\dot{X}_i$, and K^aX_i of the numerical substructure and the inertia force $M^a\ddot{X}_i$ and damping force $C_e\dot{X}_i$ of the experimental substructure are obtained using the OpenSees simulation, while the restoring force K^eX_i of the experimental substructure needs to be measured during the test.

Communication between OpenSees and the test loading equipment is realized using an establishing test element in the OpenFresco test platform (Stojadinovic *et al.* 2006, Schellenberg *et al.* 2009). The test element is an important module in OpenFresco and can be used to represent an

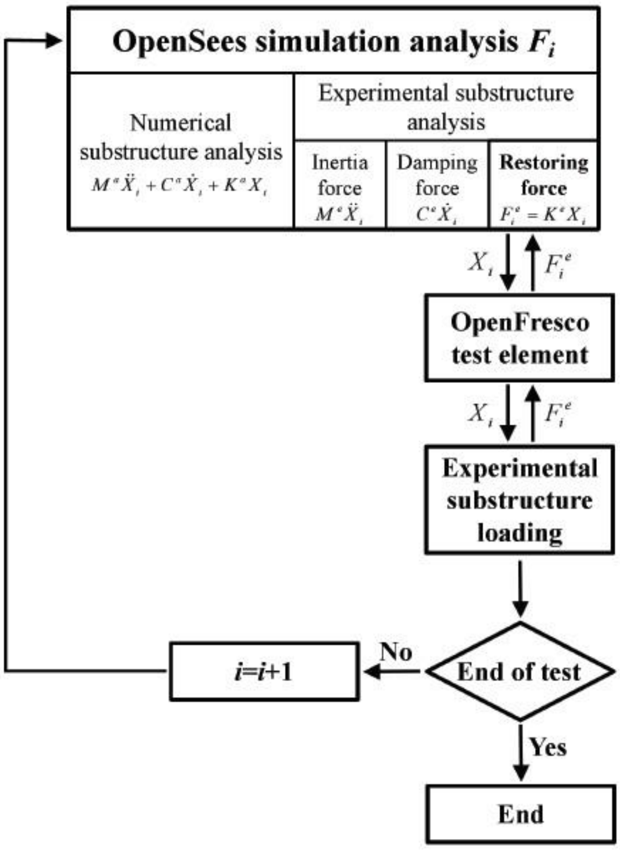

Fig. 5 SHST principle

Table 4 Cross sectional dimensions of the members

Members	Cross section size/mm
Column	H145×145×8×10
Beam	H140×100×8×10
Brace	H100×100×6×10
Shear link	H140×100×6×10

Table 5 Material properties of steel

Steel	Thickness t/mm	Yield strength f_y/MPa	Ultimate strength f_u/MPa	Elastic modulus E/(× 10^5 MPa)	Elongation δ/%
Q345B	6.08	416.2	544.08	2.12	28.46
Q345B	10.01	362.8	545.60	2.01	28.84
Q460C	8.10	475.1	634.42	2.11	25.38
Q460C	9.87	514.9	691.46	2.07	23.75

experimental substructure in the OpenFresco software system. During the test, OpenSees calculates the dynamic responses $\ddot{X}_i$, $\dot{X}_i$, and X_i of the structure at step i under the action of seismic force F_i. The displacement signal X_i is sent to the experimental substructure through the test element. The restoring force F_i^e of the experimental substructure is measured and sent back to OpenSees. Let i = i + 1, and repeat the above steps until the end of the test.

4. SHST model

In this section, the numerical substructure of the SHST is established using the FE model modeling method studied in Section 2.

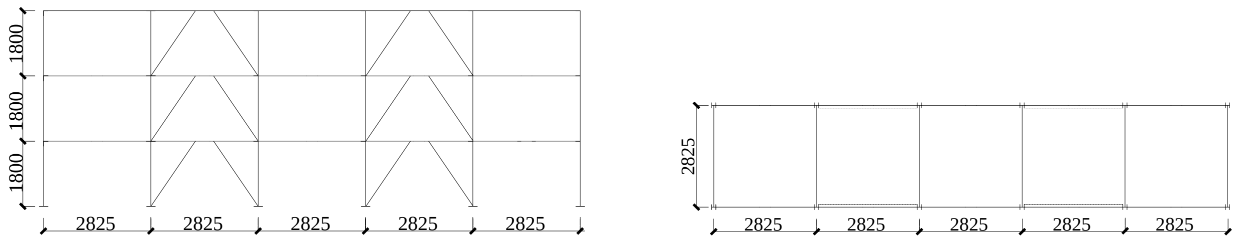

(a) Vertical view (b) Plan view

Fig. 6 Global structure model

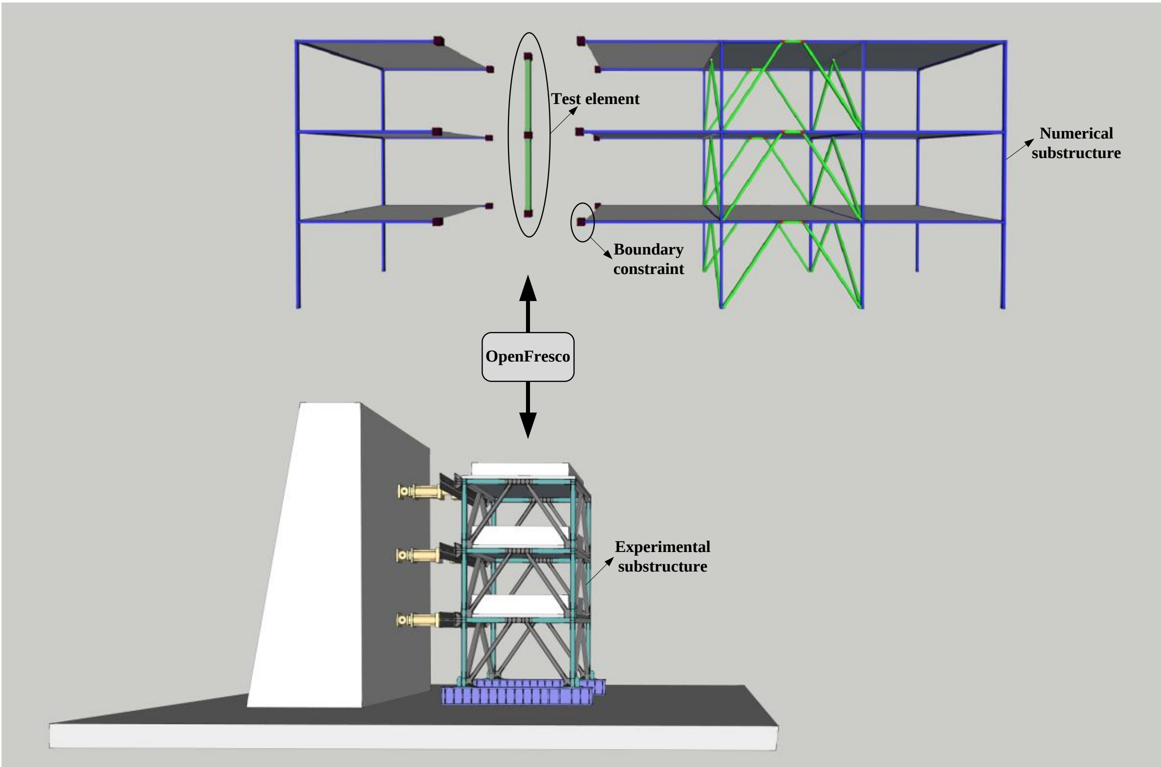

Fig. 7 Schematic diagram of SHST model

4.1 SHST model

Taking into account the actual conditions of the laboratory, a half-scale model of the prototype structure was taken as the global structural model of the SHST. The designed peak ground acceleration (PGA) of the prototype structure is 0.2 g with a 10% exceeding probability in 50 years (*Design Basis Earthquake*, DBE). As shown in Fig. 6, the model has a K-HSS-BBF structure with three stories and five spans. The height of the structure after scaling is 1800 mm, the span of two directions is 2825 mm, and the length of the shear link is 350 mm. Section dimensions of the members are listed in Table 4. The frame beam and column are made of Q460C steel, and the shear link and braces are made of Q345B steel. The material properties of the steel are listed in Table 5.

The SHST model is shown in Fig. 7. A three-story steel frame with a K-eccentric brace on the left second span is taken as the experimental substructure, and the remaining four spans are used as a numerical substructure in OpenSees to build the three-dimensional numerical model. The two substructures communicate with each other by means of a general test element in OpenFresco. The general test element is a special test element that can simulate any number of nodes and degrees of freedom.

The equivalence of the experimental substructure and the general test element is based on the floor model principle of the frame structure. The mass of each floor is equivalent to the three nodes of the test element. At the same time, it is assumed that the floor is absolutely rigid in its own plane, and only the lateral displacement of the floor is considered as the dynamic degree of freedom. The story stiffness matrix of the experimental substructure is directly obtained by the feedback displacement and force acting on the three actuators at the height of the model floor. This information is sent back to the general test element to complete the simulation analysis of the global structure model together with the numerical substructure.

Table 6 Definition parameter of shear material

Shear hinge	Steel02	Calculation	Value
Shear V_y	Yield strength f_y	$1.1aV_p$	192.88 kN
Linear stiffness K_s	Elastic modulus E	$2GA_w/e$	329.142 kN/mm
Hardening	b	—	0.02

Fig. 8 The test setup of experimental substructure

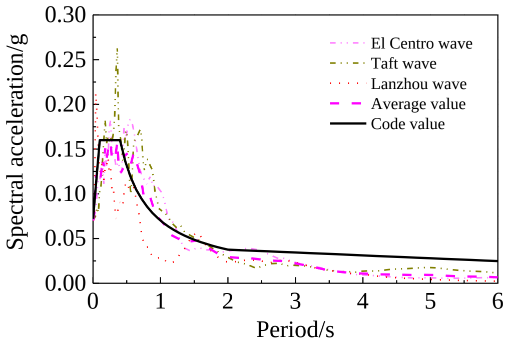

Fig. 9 Acceleration response spectra

According to the modeling study of the K-HSS-EBF in Section 2, the numerical substructure of the SHST model in this section is established. Nonlinear beam-column elements based on force are selected for frame beam-columns. Truss elements hinged at both ends are used for braces, the fiber section is selected as a cross-section type, Steel02 is selected as the material, and specific parameters are taken according to Table 5.

Simplified model in Fig. 3 is used to simulate the shear link. The shear material Steel02 is defined in the zero-length element at both ends. The specific settings are listed in Table 6.

The test setup of the experimental substructure is shown in Fig. 8. The column foot and the ground beam are connected with anchor bolts to achieve the boundary conditions of the column foot fixed-end constraint. Three MTS hydraulic servo-actuators (250 t on the first and second layers and 100 t on the third layer) are used to carry out a three-particle SHST.

The connection between the general test element and boundary node of the numerical substructure is realized by the multipoint constraint command *Multi-Point Constraint: Equal DOF* in OpenSees. The horizontal displacement of the experimental substructure and the numerical substructure in the same layer are always coordinated and unified by setting a master-slave relationship.

The load analysis is defined in OpenSees. According to the relevant provisions of GB 5011-2010, the El Centro, Taft, and Lanzhou waves are selected as the input raw seismic waves in this test. The acceleration response spectrum and average value of the three seismic waves are compared with the standard spectrum, as shown in Fig. 9.

SHST is carried out in the order of acceleration from small to large. The similarity ratio of the input seismic wave is 1.2:1 for various loading stages. The input sequence of each level of seismic wave is in the order of El Centro, Taft, and Lanzhou. The specific sequence of SHST is listed in Table 7 with a one-way loading of the seismic wave. The stiffness of the specimen is obtained by small displacement loading at the beginning of the test and at the end of each loading stage.

Table **7** Sequence of SHST

Serial number	Corresponding earthquake level	Seismic excitation	PGA/g
1		Stiffness test	
2–4	SLE[a] (intensity 7[b])	El Centro /Taft /Lanzhou waves	0.042
5		Stiffness test	
6–8	SLE (intensity 8[c])	El Centro /Taft /Lanzhou waves	0.084
9		Stiffness test	
10–12	DBE (intensity 7)	El Centro /Taft /Lanzhou waves	0.120
13		Stiffness test	
14–16	SLE (intensity 9[d])	El Centro /Taft /Lanzhou waves	0.168
17		Stiffness test	
18–20	DBE (intensity 8)	El Centro /Taft /Lanzhou waves	0.240
21		Stiffness test	
22–24	MCE[e] (intensity 7)	El Centro /Taft /Lanzhou waves	0.264
25		Stiffness test	
26–28	MCE (intensity 8)	El Centro /Taft /Lanzhou waves	0.480
29		Stiffness test	
30–32	MCE (intensity 9)	El Centro /Taft /Lanzhou waves	0.744
33		Stiffness test	
34–36		El Centro /Taft /Lanzhou waves	1.0
37		Stiffness test	

[a]*Strength Level Earthquake* with recurrence probability of 63% in 50 years.
[b]The design PGA is 0.10g. [c]The design PGA is 0.20g. [d]The design PGA is 0.40g.
[e]*Maximum Considered Earthquake* with recurrence probability of 2% in 50 years

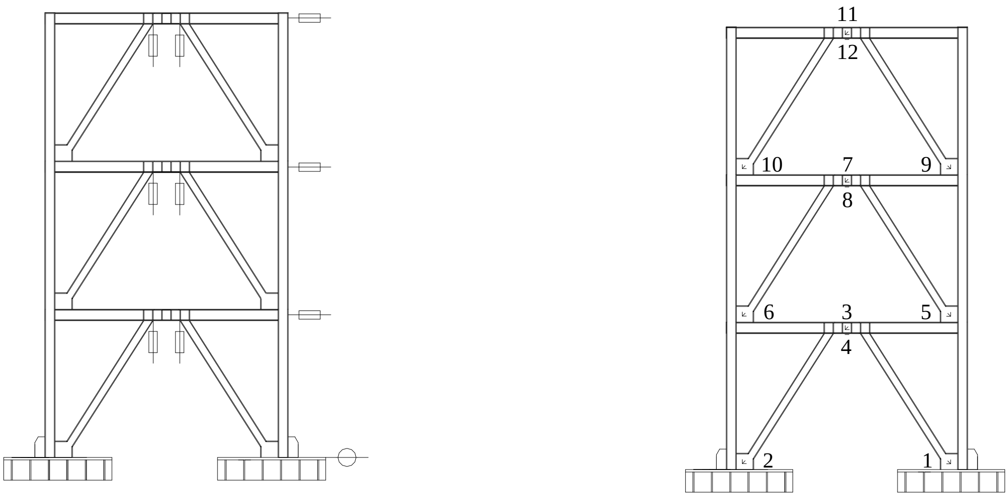

(a) Layout of linear displacement sensors (b) Layout of strain gauges

Fig. 10 Instrumentation arrangement of the experimental substructure

4.2 Experimental substructure measurement scheme

As shown in Fig. 10(a), the top displacement, interstory drift, column foot displacement, and rotation of the shear link of the experimental substructure are measured by linear displacement sensors. The strain of the substructure is measured by resistance strain gauges. As shown in Fig. 10(b), the strain gauges are arranged at the flange of the shear link, and the strain rosettes are arranged at the column foot, beam-column panel zone, and web of the shear link.

4.3 Global numerical model of structure

A pure numerical model of the global structure is established and is mainly used for comparison with subsequent SHST results. As shown in Fig. 11, the models

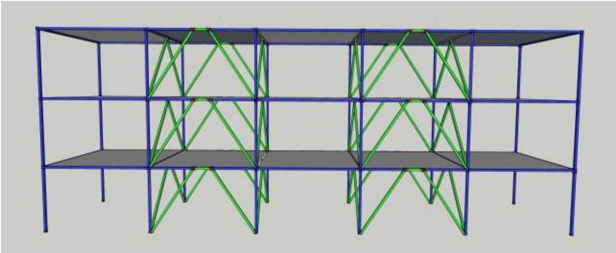

Fig. 11 Global numerical model of the structure

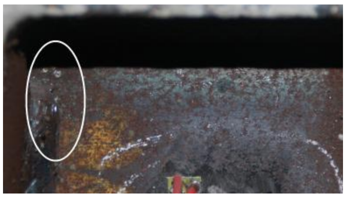

(a) Peeling phenomenon of shear link

(b) Transverse crack of floor slab

(c) Transverse short cracks of floor slab

(d) Floor gaps in shear links

(e) Floor slab crack

(f) Partial crushing of floor slab

Fig. 12 Test phenomena

Table 8 Test phenomena

Cases	PGA/g	Description
10-13	0.120	The first noise came from the model.
18-20	0.240	Slight rust peeling occurred at the junction of stiffening rib and flange of the first and second storeys of the model's northern shear link. A slight peeling phenomenon occurred at the weld between the web and stiffener ribs of the shear link as shown in Fig. 12(a).
26-28	0.480	Transverse cracks appeared on the upper floor of the shear link on both sides of the first floor of the model as shown in Fig. 12(b); short transverse cracks appeared on the upper floor of the shear link on the south side of the second floor as shown in Fig. 12(c); obvious gaps appeared between the floor and upper flange of shear link at the same position as shown in Fig. 12(d).
30-32	0.744	Transverse cracks appeared on the upper floor of the second floor shear link on the south side of the model, and obvious cracks appeared on the lower side of the first and second floor as shown in Fig. 12(e).
34-36	1.0	The floor slab of the first floor in the north was partially crushed as shown in Fig. 12(f), and more long cracks appeared at the bottom of the first and second floor.

of columns, beams, braces, and shear links are consistent with the numerical substructures in the SHST model.

5. Test phenomenon

Under the action of three kinds of seismic waves, the damage to the experimental substructure first occurred at the shear link, which is consistent with the design. With an increase in the peak value of the seismic load, the floor slab cracked near the shear link of the first and second floors. It is clear that the deformation is mainly concentrated at the shear link of each floor. At the same time, the shear link was restrained by the floor during the deformation process, and the floor itself was also squeezed. During the entire test loading process, no irreversible deformation characteristics such as local buckling or instability occurred in the beam, column, brace, or shear link of the frame. Table 8 lists the test phenomena observed for different cases.

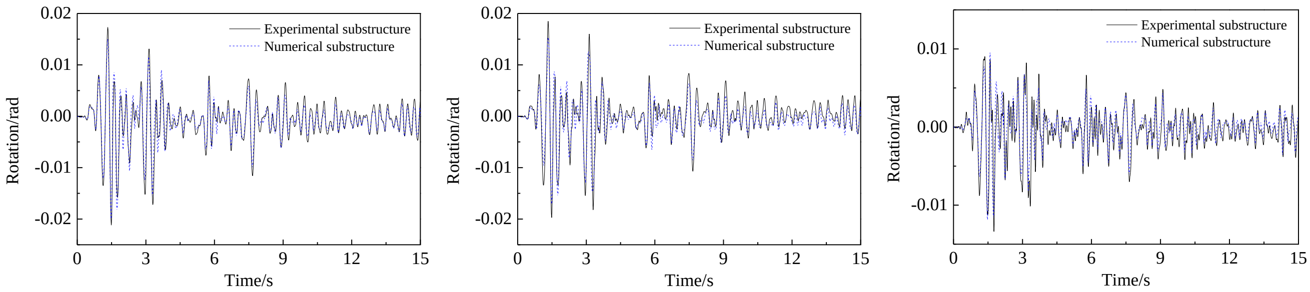

(a) PGA=0.744 g, first floor (b) PGA=0.744 g, second floor (c) PGA=0.744 g, third floor

Fig. 13 Time-history-curves of shear link rotation

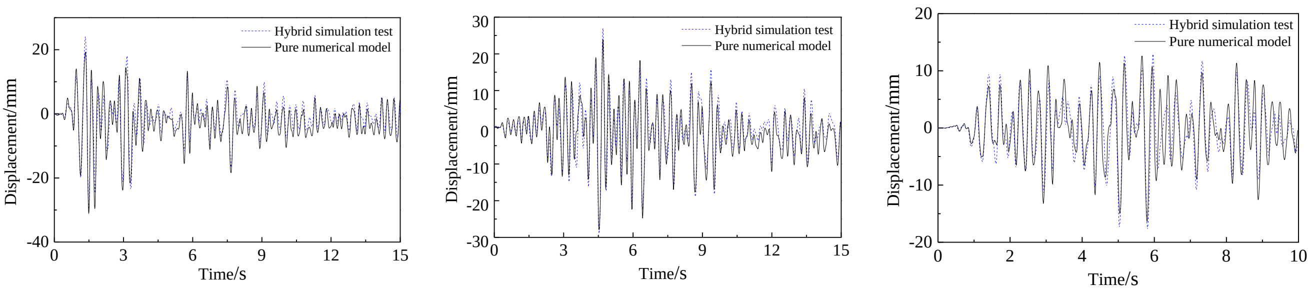

(a) El Centro wave (b) Taft wave (c) Lanzhou wave

Fig. 14 Time-history-curves of displacement

6. Validation of SHST model

6.1 Substructure comparison

Comparisons of the time-history-curves of the rotations of the third-story shear links are shown in Fig. 13 for the experimental and numerical substructures under the action of the El Centro wave with an MCE (intensity 9). The time transverse axis of the experimental substructure is adjusted according to the test data in order to correspond with the numerical substructure. It can be seen that the link rotations of the experimental and numerical substructures are comparatively consistent.

Near the maximum acceleration peak, the coincidence decreases slightly, and the maximum relative error is -12.3%. This is mainly caused by the actual measurement error of the experimental substructure and the neglect of the restraint effect of the stiffeners and concrete floors when modeling the SHST model.

6.2 Global structure comparison

Fig. 14 shows the a time-history-curve comparison of the top floor command displacement of the SHST model, and the calculation displacement of the global structure pure numerical model under MCE (intensity 9). It can be seen that the experimental results of the SHST model under seismic load are basically consistent with the results of the global structure pure numerical model using OpenSees with a maximum relative error of 13.5%. Because the restraint of the floor to the beam is considered in the space frame, the absolute rigidity of the floor in its own plane is basically guaranteed during the entire test process. Therefore, only the horizontal degree of freedom of the experimental substructure is considered in the SHST model, which has little influence on the accuracy of the SHST results.

7. Structural seismic performance analysis

7.1 Global structure displacement response

The maximum displacement of each layer relative to the base of the SHST model is shown in Fig. 15. It can be seen that the displacement response of the model structure under three kinds of seismic waves is an inverse triangle distribution. The displacement response of the El Centro wave is the largest, and that of the Lanzhou wave is the smallest. Under SLEs, the relative lateral displacement of each layer of the model is not obvious, which indicates that the overall displacement response of the structure is small. However, after the MCE (intensity 8) loading stages, the maximum relative displacement of each floor changes significantly.

Table 9 lists the maximum interstory drifts of each story in the SHST model under different loading stages. It can be seen that the maximum interstory drift appears on the first story. According to the calculation results, the maximum interstory drifts of the model structure under SLEs and MCEs are 1/409 and 1/95, respectively. These values satisfy

Table 9 Maximum inter-story drifts of SHST model

PGA/g	0.042	0.084	0.120	0.168	0.240	0.264	0.480	0.744	1.0
1st floor	1/4204	1/1559	1/1116	1/701	1/455	1/409	1/208	1/129	1/95
2nd floor	1/4859	1/1839	1/1203	1/818	1/580	1/514	1/227	1/136	1/110
3rd floor	1/5893	1/3000	1/1636	1/1058	1/659	1/620	1/321	1/268	1/258

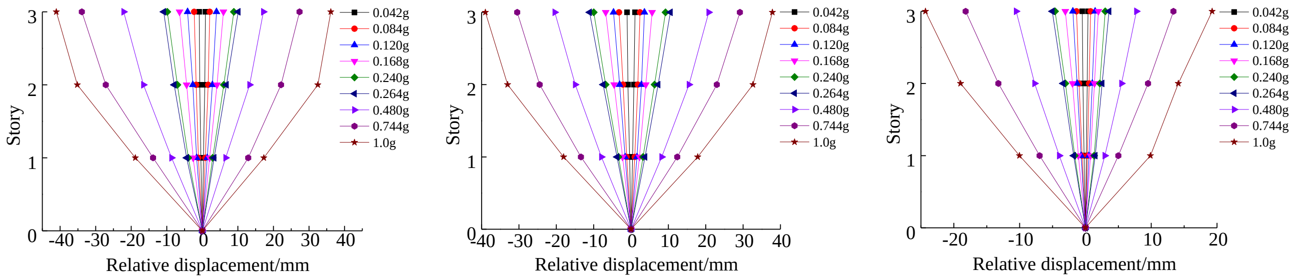

(a) El Centro wave (b) Taft wave (c) Lanzhou wave

Fig.15 Maximum relative displacement of SHST model

Table 10 Natural frequencies of the experimental substructure

Sequence	1	5	9	13	17	21	25	29	33	37
Natural frequency/Hz	6.328	6.320	6.321	6.295	6.267	6.243	6.232	6.174	6.085	5.975

the requirements for the limit values of the elastic and elastic-plastic interstory drifts of multistory and high-rise steel structures in GB 50011-2010.

7.2 Experimental substructure analysis

7.2.1 Stiffness degradation

The analysis function program is established by using MATLAB. By inputting a stiffness test matrix and mass matrix, the natural frequencies of the model under various loading stages can be calculated, as shown in Table 10. The results indicate that the basic natural frequency of the experimental structure is 6.328 Hz. With an increase in the acceleration peak of the seismic wave, the overall response of the model becomes larger. Transverse cracks and surface cracks appear in the concrete floor, and the deformation of the shear links leads to a decrease in the stiffness of the structure, an increase in the period, and a decrease in the natural frequency.

Fig. 16 shows the stiffness degradation rate curve of the model structure. It can be seen that the maximum stiffness degradation rate of the model is 10.823%. After SLEs, the stiffness of the model changes little compared with the initial stiffness, indicating that the structure is still in an elastic state, which is basically consistent with the experimental phenomena. When the input acceleration peak reaches the MCE (intensity 9) level, the stiffness decreases more significantly, indicating that damage accumulation occurs in the model.

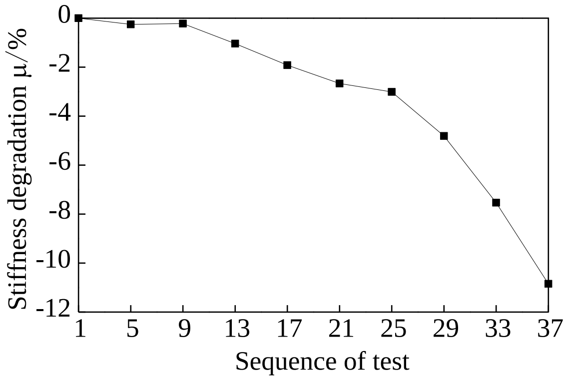

Fig. 16 Stiffness degradation of the experimental substructure

7.2.2 Horizontal seismic force

According to the feedback forces of the three actuators and the output results of the response force of the general test element, the horizontal seismic forces of each floor of the experimental substructure under different loading stages are obtained. As shown in Fig. 17, the horizontal seismic force on the first floor of the model is the smallest, and that on the third floor is the largest. These forces are roughly distributed in an inverted triangle, indicating that the structure is mainly experiencing shear deformation. Under the action of SLEs, the horizontal seismic actions of each

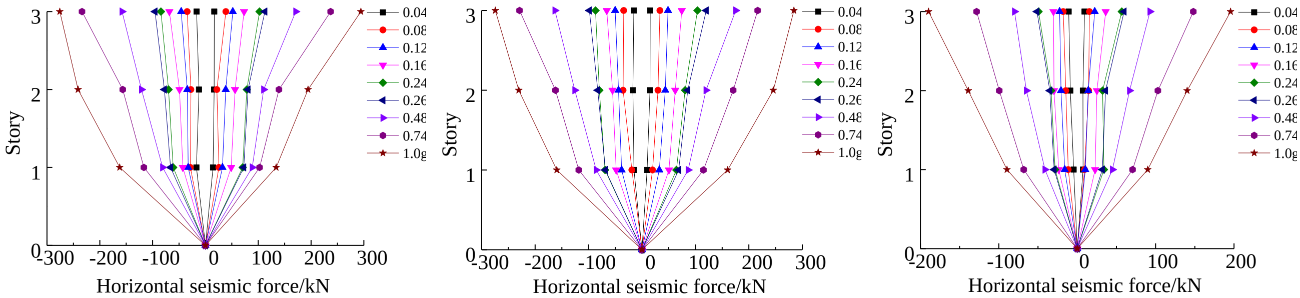

(a) El Centro wave (b) Taft wave (c) Lanzhou wave

Fig. 17 Horizontal seismic force of the experimental substructure

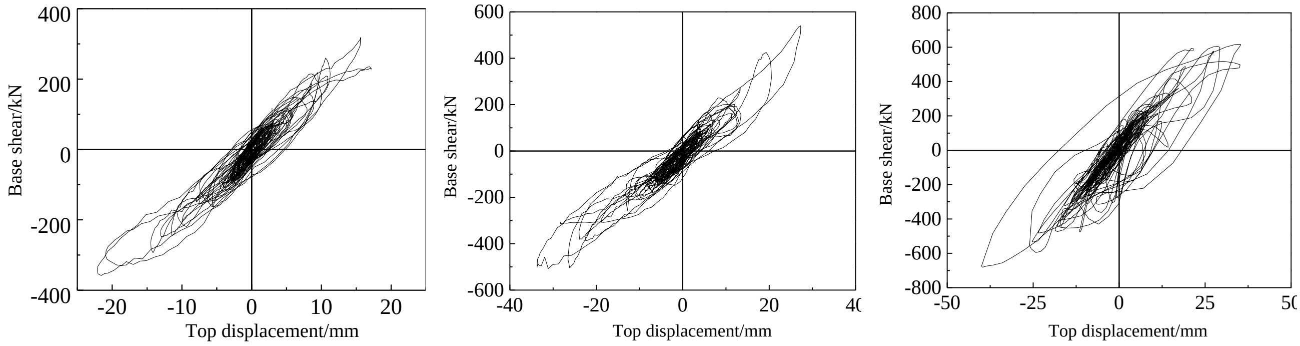

(a) PGA=0.480 g (b) PGA=0.744 g (c) PGA=1.0 g

Fig. 18 Hysteretic loops of base shear vs. top displacement

layer do not differ significantly. With an increase in the PGA of the seismic wave, the horizontal seismic forces of each floor increase by varying degrees and the growth trends are relatively close, indicating that the stiffness of the specimen changes little.

7.2.3 Hysteretic loops

Fig. 18 shows the base shear vs. top displacement hysteretic loops of the model under the action of El Centro waves. During the MCE (intensity 8) loading stage, the model is basically in the elastic state, and the hysteretic loop is kept in a straight line. After the MCE (intensity 9), cracks in the concrete floor make the nonlinear characteristics of the model more obvious. When the PGA reaches 1.0 g, the model enters into plasticity and forms hysteretic loops.

Fig. 19 shows the story shear vs. interstory drift hysteretic loops of the model under the action of El Centro waves. It can be seen that under the MCE (intensity 8) loading stage, the structure of each story is basically in the elastic stage, with almost no dissipated energy, and the hysteretic loops are almost straight lines, and the surrounding area is very small. Under the MCE (intensity 9) loading stage, the third floor of the structure is in the elastic domain, and the first and second floors of the structure have the tendency of entering the plastic domain. When the PGA reaches 1.0 g, the third floor of the structure is still in the elastic stage, hysteretic loops appear on the first and second floors of the structure, and the changes on the first floor are more obvious than those on the second floor.

7.2.4 Skeleton curves

Fig. 20 shows the skeleton curves of each story of the SHST model under different intensity El Centro waves. The characteristic points of the skeleton curves are obtained according to the envelope of the hysteretic loops under different loading conditions. Before the MCE (intensity 8) loading stage, each story of the SHST model is in the elastic stage, and there are linear changes between the inter-story drift and the story shear. After the MCE (intensity 8) loading stage, because the first and second stories of the model bear larger horizontal shear force, the first and second layers begin to enter the elastic-plastic state, and the slope of the skeleton curves decrease. At the same time, it is observed that the third story is still basically in the elastic state. When the PGA reaches 1.0 g, the inter-story drift of the first story of the model has reached 18.95 mm. At this time, the stiffness of the first and second stories of the model decreases more obviously, and the third story also tend to enter the elastic-plastic deformation.

Table 11 summarizes the characteristic point parameters of skeleton curves and ductility factors of each story. Since there is no obvious descending section in the skeleton curve, the ultimate point is the peak point of the maximum loading stage. The yielding displacement of each story of the SHST model is close to each other. The ductility factor

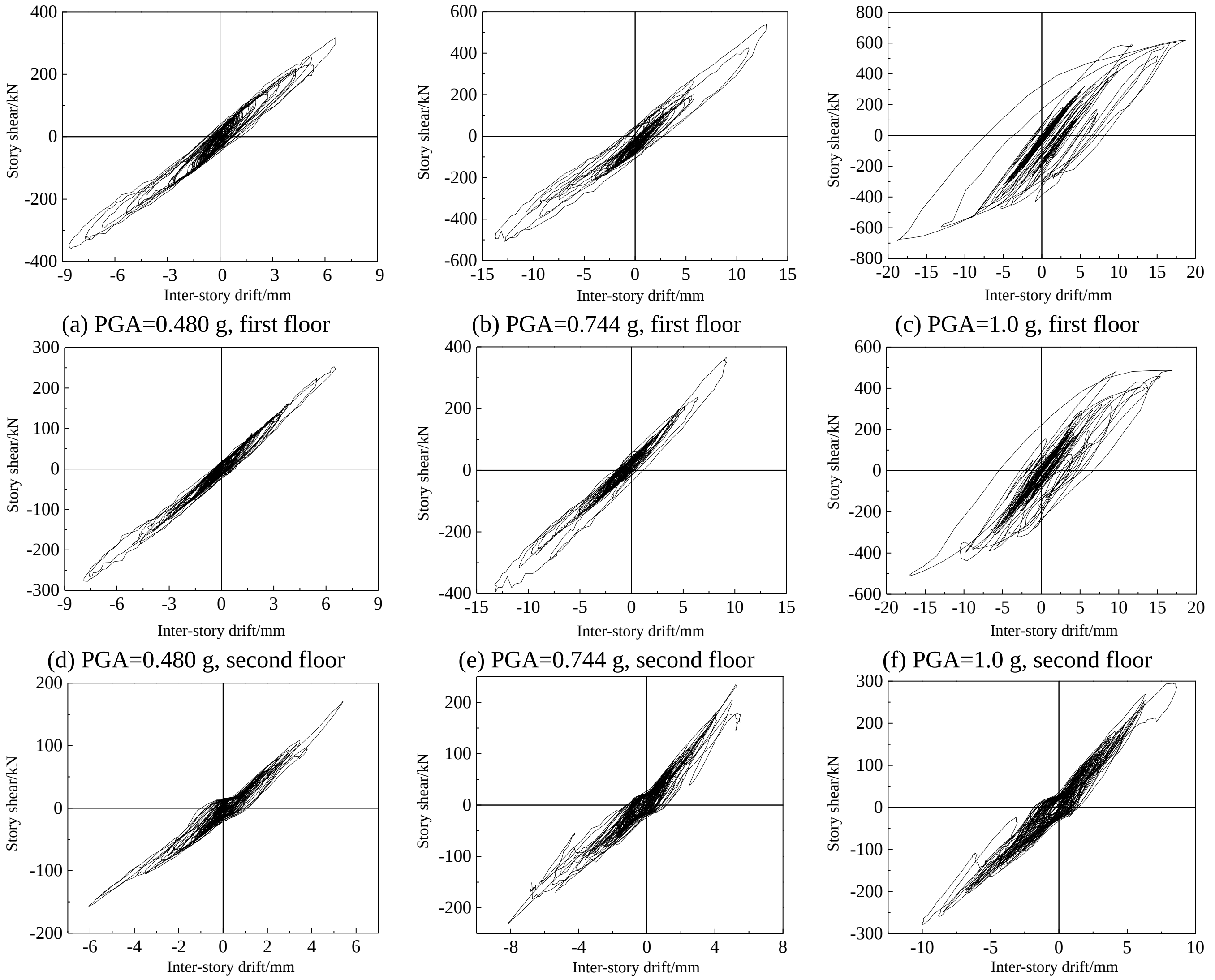

(a) PGA=0.480 g, first floor (b) PGA=0.744 g, first floor (c) PGA=1.0 g, first floor

(d) PGA=0.480 g, second floor (e) PGA=0.744 g, second floor (f) PGA=1.0 g, second floor

(g) PGA=0.480 g, third floor (h) PGA=0.744 g, third floor (i) PGA=1.0 g, third floor

Fig. 19 Hysteretic loops of story shear vs. inter-story drift

Table 11 Characteristic points of skeleton curves and ductility factor

Position	Loading direction	Yield point		Ultimate point		Ductility $\mu = \Delta_u / \Delta_y$
		Drift Δ_y/mm	Shear F_y/kN	Drift Δ_u/mm	Shear F_u/kN	
First story	Positive	4.282	305.661	17.662	618.378	4.126
	Negative	-4.482	-271.522	-18.716	-676.187	4.176
Second story	Positive	3.796	201.653	15.223	485.974	4.010
	Negative	-3.609	-175.988	-16.302	-507.823	4.517
Third story	Positive	4.244	147.823	8.607	295.761	2.028
	Negative	-4.191	-129.161	-10.061	-283.443	2.401

is the ratio of the ultimate inter-story drift to the yield inter-story drift. It can be observed that the ductility factors of the first and second stories of the SHST model have exceeded 4, which indicates that the Y-HSS-EBF model exhibits good ductility in the elastic-plastic stage.

7.2.5 Cumulative energy dissipation time-history response

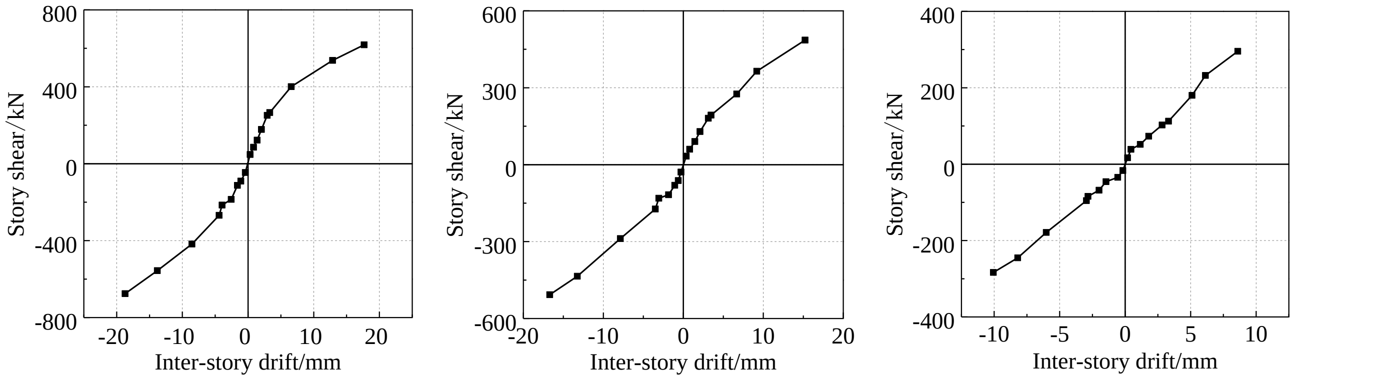

(a) First story (b) Second story (c) Third story

Fig. 20 Skeleton curves

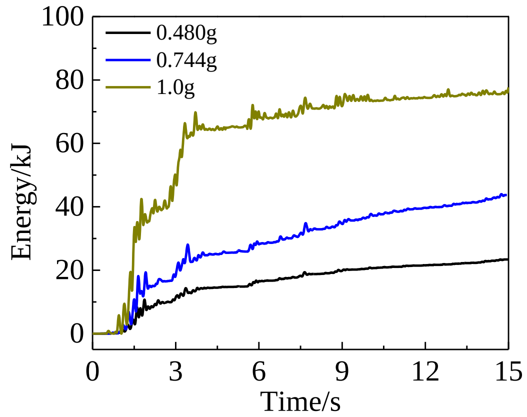

Fig. 21 Cumulative energy dissipation time-history responses of the experimental substructure

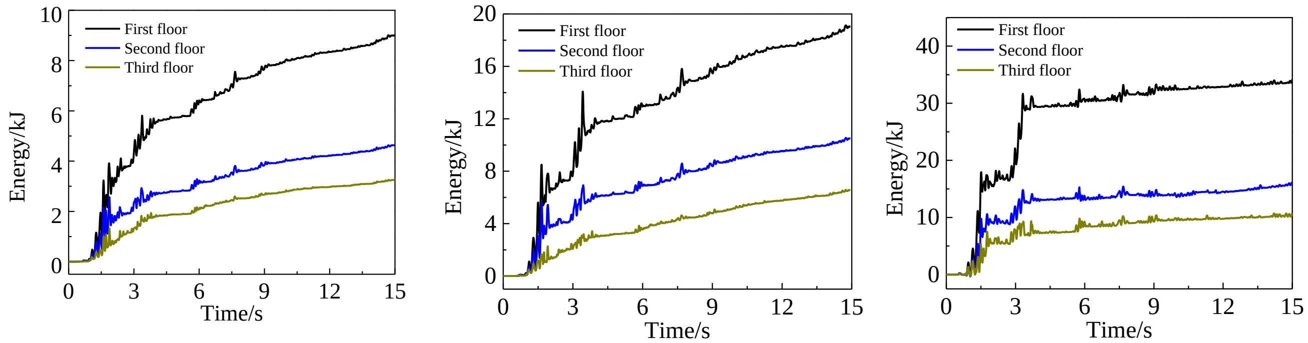

(a) PGA=0.480 g (b) PGA=0.744 g (c) PGA=1.0 g

Fig. 22 Time-history responses of cumulative energy dissipation at different stories

Energy dissipation is one of the important indexes that reflect the seismic performance of structures. As shown in Fig. 21, the cumulative energy dissipation time-history responses of the experimental substructure under different intensities of El Centro waves are obtained according to the hysteretic loops of the base shear and top displacement. It can be seen that when the PGA of the input seismic wave is 0.480 g and 0.744 g, the overall cumulative energy dissipation of the model is small, the model is basically in the elastic domain, and the hysteretic energy consumption mainly comes from the elastic strain energy. Thus, the overall cumulative energy dissipation time-history responses show a wavelike growth. When the PGA reaches 1.0 g, the fluctuation value of the energy dissipation response of the structure shows a great leap. The deformation of the shear links and more cracks in the floor make the plastic damage of the structure accumulate continuously, which indicates that the model moves from the elastic to the elastic-plastic domain.

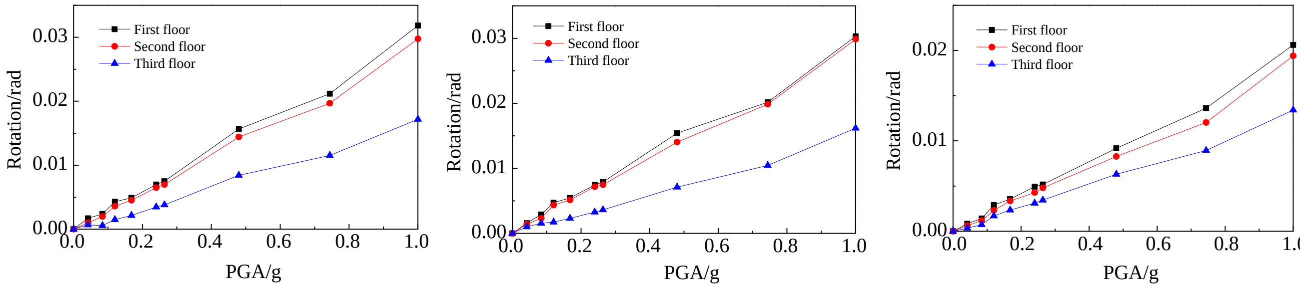

(a) El Centro wave (b) Taft wave (c) Lanzhou wave

Fig. 23 Maximum rotations of the shear links

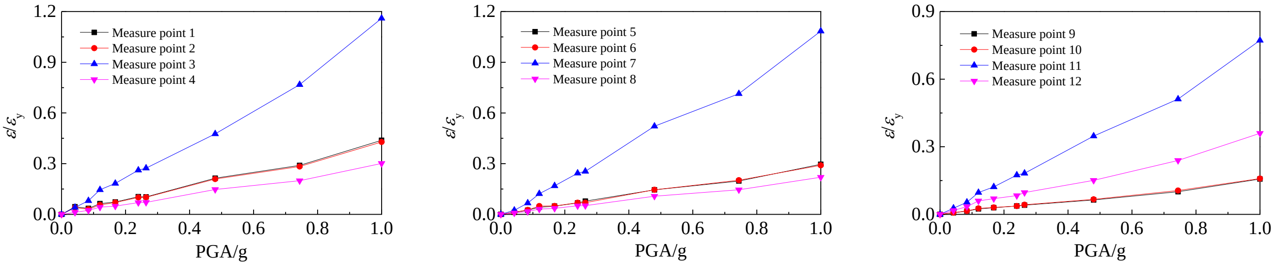

(a) The first floor (b) The second floor (c) The third floor

Fig. 24 Variation of strain of the experimental substructure

As shown in Fig. 22, the cumulative energy dissipation time-history responses of each layer under different intensities of El Centro waves are obtained according to the hysteretic loops of the story shear and interstory drift. It can be seen that the energy consumption of the first layer of the model is the largest and that of the third layer is the smallest, which is consistent with the experimental phenomena. The growth trend of energy consumption in each layer is basically consistent with the overall energy consumption. When the PGA reaches 1.0 g, the energy consumption in each layer increases significantly.

Table 12 summarizes the cumulative total energy consumption of the experimental substructure. It can be seen that when the PGA reaches 1.g, the cumulative total energy dissipation of the global experimental substructure exceeds the sum of the total energy dissipation of the other loading stages, which indicates that the model undergoes greater elastic-plastic deformation under the action of the exceeding MCE (intensity 9). The deformation and energy dissipation of the experimental substructure mainly occur in the first story, and the dissipated energy is close to 50% of the total energy dissipated by the model.

7.2.6 Rotations of shear link

Fig. 23 shows the rotations of the shear links under different loading stages. The rotation of the first-floor shear link is the largest, and the value of the third-floor shear link is the smallest, which is also consistent with the displacement response of the floor. Before the MCE (intensity 8) loading stage, the rotation of shear link increases slowly, and the maximum value is less than 0.01 rad. After the MCE (intensity 8) loading stage, the breakline slope increases obviously because of the degradation of the model stiffness. The maximum rotation of the shear link is 0.033 rad after the El Centro wave with an acceleration of 1.0 g, which is less than the limit value of the shear yield link of AISC341-16 (2016) with $\gamma_p \leq 0.08$ rad.

7.2.7 Strain response analysis

Fig. 24 shows the measured strain response of each floor under the El Centro wave. The corresponding strain $\varepsilon/\varepsilon_y$ in the figure is the ratio of measured strain ε to yield strain ε_y. It can be seen that the strain at the web of the shear link (measured points 3, 7, 11) is obviously higher than that at other measured points, which indicates that the structure mainly depends on the shear deformation of the web of the link in order to dissipate energy. The strain value of each measuring point increases steadily, and the difference is small from the SLE (intensity 7) to MCE (intensity 7) cases. After the MCE (intensity 8) loading stage, the strain value of each measuring point increases obviously, especially at the web of the shear link (measured points 3, 7, 11). When the PGA reaches 1.0 g, the strain at the web of the first- and second-floor shear links (measured points 3, 7) exceeds the yield strain ($\varepsilon/\varepsilon_y > 1$), which indicates that the webs of the shear links enter the plastic dissipated seismic energy.

As observed in Fig. 24(a), the stiffness of the bottom floor is improved because of the rigid connection between the column foot and the ground beam. The stiffening plate is set on the flange of the column foot, so the panel zone at the column foot also shares more earthquake force (measured points 1–2). Fig. 24(b) shows that the deformation of the second floor is mainly concentrated in the web of the shear link, and the strain in the beam-column panel zone and the flange of the shear link is small. The seismic response of all measured points on the third floor is small and does not yield.

8. Conclusions

Using the FE software OpenSees and the OpenFresco-based SHST system, the seismic behavior of the K-HSS-EBF was further investigated. The following conclusions can be drawn from this research:

(1) A numerical model corresponding to the existing experimental model was established using OpenSees. The numerical model was verified by comparing the hysteretic loops of the two models, which showed that OpenSees can effectively simulate the numerical substructure model of the K-HSS-EBF.

(2) Based on the floor model principle of the frame structure, the method of using the general test element in OpenFresco to equivalent the experimental substructure of a three stories space frame has been proved to be reasonable. In the spatial SHST, the results of the SHST model were in good agreement with those of the global structure pure numerical model under MCE (intensity 9) loading stages. It could be seen that the SHST method based on OpenFresco had good stability and accuracy.

(3) Under three kinds of seismic waves, the displacement response of the SHST model presented an inverted triangle distribution. The maximum interstory drifts of the model structure under SSLEs and MCEs were 1/409 and 1/95, respectively, which conformed to the limit of the seismic design code.

(4) The hysteretic loops of the storey shear versus the inter-story drift and cumulative energy dissipation indicated that the deformation and energy dissipation of the experimental substructure mainly occur in the first story, and the dissipated energy is close to 50% of the total energy dissipated by the model.

(5) The rotation of the shear link increased with the PGA and decreased with increasing height. After the model entered the elastic-plastic state, the energy dissipation mainly depended on the deformation of the shear links, and more cracks occurred in the floor. The maximum strain of links occurred on the web, which indicates that shear deformation occurs mainly in the link section.

Acknowledgments

The research described in this paper was financially supported by the National Natural Science Foundation of China (Grant No. 51178382).

References

AISC341-16 (2016), Seismic Provision for Structure Steel Buildings, American Institute of Steel Construction; Chicago, USA.

Alhendi, H. and Celikag, M. (2015), "Behavior of reverse-channel and double-reverse-channel connections to tubular columns with HSS", *J. Constr. Steel Res.*, **112**, 271-281. https://doi.org/10.1016/j.jcsr.2015.05.017.

Aslani, F., Uy, B., Wang, Z. and Patel, V. (2016), "Confinement models for high strength short square and rectangular concrete-filled steel tubular columns", *Steel Compos. Struct.*, **22**(5), 937-974. https://doi.org/10.12989/scs.2016.22.5.937.

Ban, H.Y., Shi, G., Shi, Y.J. and Wang, Y.Q. (2013), "Residual stress of 460 MPa high strength steel welded box section: experimental investigation and modeling", *Thin-Walled Struct.*, **64**, 73-82. https://doi.org/10.1016/j.tws.2012.12.007.

Berman, J.W. and Bruneau, M. (2008), "Tubular Links for Eccentrically Braced Frames. I: Finite Element Parametric Study", *J. Struc. Eng.*, **134**(5), 692-701. https://doi.org/10.1061/(ASCE)0733-9445(2008)134:5(692).

Bosco, M. and Rossi, P.P. (2009), "Seismic behaviour of eccentrically braced frames", *Eng. Struct.*, **31**(3), 664-674. https://doi.org/10.1016/j.engstruct.2008.11.002.

Bosco, M. and Rossi, P.P. (2013), "A design procedure for dual eccentrically braced systems: analytical formulation", *J. Constr. Steel Res.*, **80**(1), 440-452. https://doi.org/10.1016/j.jcsr.2012.09.019.

Chae, Y., Ricles, J.M. and Sause, R. (2015), "Large-scale real-time hybrid simulation of a three-story steel frame building with magneto-rheological dampers", *Earthq. Eng. Struct. D.*, **43**(13), 1915-1933. https://doi.org/10.1002/eqe.2429.

Dermitzakis, S.N. and Mahin, S.A. (1985), "Development of substructuring techniques for on-line computer controlled seismic performance testing", Research Report No.UCB/EERC-85/04; Earthquake Engineering Research Center, Berkeley, CA.

Dubina, D., Stratan, A. and Dinu, F. (2008), "Dual high-strength steel eccentrically braced frames with removable links", *Earthq. Eng. Struct. D.*, **37**(15), 1703-1720. https://doi.org/10.1002/eqe.828.

Fu, B., Jiang, H.J. and Wu, T. (2019), "Experimental study of seismic response reduction effects of particle damper using substructure shake table testing method", *Struct. Control Health Monit.*, **26**(2), e2295. https://doi.org/10.1002/stc.2295.

GB 50011-2010 (2016 edition) (2016), Code for seismic design of buildings, China Architecture and Building Press, Beijing, China.

Ioana, A., Stratana, A., Dubinǎa, D., Poljanšekc, M., Taucerc, F., Pegonc, P. and Sabǎu, G. (2016), "Experimental validation of re-centering capability of eccentrically braced frames with removable links", *Eng. Struct.*, **113**(15), 335-346. https://doi.org/10.1016/j.engstruct.2016.01.038.

Khan, M.A., Jiang, L., Cashell, K.A., and Usmani, A. (2018), "Analysis of restrained composite beams exposed to fire using a hybrid simulation approach", *Eng. Struct.*, **172**, 956-966. https://doi.org/10.1016/j.engstruct.2018.06.048.

Kim, D.K., Lee, C.H., Han, K.H., Kim, J.H., Lee, S.E. and Sim, H.B. (2014), "Strength and residual stress evaluation of stub columns fabricated from 800 MPa high-strength steel", *J. Constr. Steel Res.*, **102**, 111-120. https://doi.org/10.1016/j.jcsr.2014.07.007.

Li, S., Liu, Y.H. and Tian, J.B. (2018), "Experimental and Analytical Study of Eccentrically Braced Frames Combined with High-Strength Steel", *Int. J. Steel Struct.*, **18**, 528-553. https://doi.org/10.1007/s13296-018-0018-x.

Li, T.F., Su M.Z. and Sui Y. (2019), "Numerical modeling of high-strength steel composite K-eccentrically braced frames and spatial substructure hybrid simulation tests", *B. Earthq. Eng.*, **17**(11), 6239-6263. https://doi.org/10.1007/s10518-019-00720-2.

Li, T.F., Su M.Z., and Sui Y. (2020), "Spatial substructure hybrid simulation tests of high-strength steel composite Y-eccentrically braced frames", *Steel Compos. Struct.*,**34**(5), 715-732. https://doi.org/10.12989/scs.2020.34.5.715.

Lian, M., Su, M.Z. and Guo, Y. (2015), "Seismic performance of eccentrically braced frames with high strength steel combination", *Steel Compos. Struct*., **18**(6), 1517-1539. https://doi.org/10.12989/scs.2015.18.6.1517.

Mazzoni, S., McKenna, F., Scott, M.H. and Fenves, G.L. (2009), *Open system for earthquake engineering simulation user command-language manual—OpenSees version 2.0*, Pacific Earthquake Engineering Research Center (PEER), Univ. of California, Berkeley, CA, USA.

Menegotto, M. and Pinto, E. (1973), "Method of analysis for cyclically loaded RC plane frames including changes in geometry and non-elastic behavior of elements under combined normal force and bending", *IABSE symposium on resistance and ultimate deformability of structures acted on by well defined repeated loads*, Lisbon, Portual, 15-22.

Montuori, R., Nastri, E. and Piluso, V. (2014), "Theory of plastic mechanism control for eccentrically braced frames with inverted y-scheme", *J. Constr. Steel Res.*, **92**(1), 122-135. https://doi.org/10.1016/j.jcsr.2013.10.009.

Özhendekci, D. and Özhendekci, N. (2008). "Effects of the frame geometry on the weight and inelastic behaviour of eccentrically braced chevron steel frames", *J. Constr. Steel Res.*, **64**(3), 326-343. https://doi.org/10.1016/j.jcsr.2007.07.009.

Schellenberg, A., Kim, H.K., Takahashi, Y., Fenves, G.L. and Mahin, S.A. (2009), *OpenFresco Command Language Manual*, The Regents of the University of California, CA, USA, 38-39.

Shayanfar, M.A., Barkhordari, M.A. and Rezaeian, A.R. (2011), "Experimental study of cyclic behavior of composite vertical shear link in eccentrically braced frames", *Steel Compos. Struct.*, **12**(1), 13-29. http://dx.doi.org/10.12989/scs.2011.12.1.013.

Shi, G., Liu, Z., Ban, H.Y., Zhang, Y., Shi, Y.J. and Wang, Y.Q. (2012), "Tests and finite element analysis on the local buckling of 420 MPa steel equal angle columns under axial compression", *Steel Compos. Struct.*, **12**(1), 31-51. http://dx.doi.org/10.12989/scs.2011.12.1.031.

Stojadinovic, B., Mosqueda, G. and Mahin, S.A. (2006), "Event-driven control system for geographically distributed hybrid simulation", *J. Struct. Eng.*, **132**(1), 68-77.

Tian, X.H., Lian, M., Su, M.Z., Wang, F. and Li, S. (2018), "Seismic behavior of K-shaped eccentrically braced frames with high-strength steel: Shaking table testing and FEM analysis", *J. Constr. Steel Res.*, **143**, 250-263. https://doi.org/10.1061/(ASCE)0733-9445(2006)132:1(68).

Wang, F., Su, M.Z., Hong, M., Guo, Y.R. and Li, S.H. (2016), "Cyclic behaviour of Y-shaped eccentrically braced frames fabricated with high-strength steel composite", *J. Constr. Steel Res.*, **120**(2), 176-187. https://doi.org/10.1016/j.jcsr.2016.01.007.

Wang, T., Mosqueda, G., Jacobsen, A. and Cortes-Delgado, M. (2012), "Performance evaluation of a distributed hybrid test framework to reproduce the collapse behavior of a structure", *Earthq. Eng. Struct. D.*, **41**(2), 295-313. https://doi.org/10.1002/eqe.1130.

Wu, B., Chen, Y.S., Xu, G.S., Mei, Z., Pan, T.L. and Zeng, C. (2016), "Hybrid simulation of steel frame structures with sectional model updating", *Earthq. Eng. Struct. D.*, **45**(8), 1251-1269. https://doi.org/10.1002/eqe.2706.

Yang, W.X. (2011), "Seismic Response Modification Factor of Y-eccentrically Braced Steel Frame Structures", Ph.D. Dissertation, Shanghai Jiao Tong University, Shanghai, China.

CC